Nanoscale

PAPER

View Article Online
View Journal | View Issue

Check for updates

Cite this: *Nanoscale*, 2022, **14**, 11568

Rationally designed nanoarray catalysts for boosted photothermal CO_2 hydrogenation†

Xukai Shen,[a] Chaoran Li, *[a,b] Zhiyi Wu,[a] Rui Tang,[a] Jiahui Shen,[a] Mingyu Chu,[a] Ao-Bo Xu,[a] Bingchang Zhang, *[c] Le He *[a,b] and Xiaohong Zhang [a,b]

Received 15th May 2022,
Accepted 15th July 2022

DOI: 10.1039/d2nr02680e

rsc.li/nanoscale

It is of emerging interest to convert CO_2 and green H_2 into solar fuels with great efficiency through photothermal CO_2 hydrogenation. However, designing photothermal catalysts with improved sunlight harvesting ability, intrinsic catalytic activity, and thermal management to prevent heat dissipation still remains rather challenging. Herein, we report a facile structural engineering strategy for preparing efficient nanoarray-based photothermal catalysts with strong light absorption ability, high metal dispersity, and effective thermal management. Optimizing the 120 μm-SiNCs@Co catalyst allowed it to reach a record high Co-based photothermal CO_2 conversion rate of 1780 mmol g_{Co}^{-1} h^{-1}. This study provides insight into the structural engineering of photothermal catalysts for enhanced catalytic performance and lays a foundation for efficient photothermal CO_2 catalysis.

Published on 19 July 2022. Downloaded on 5/31/2024 7:48:38 PM.

Introduction

Photothermal CO_2 hydrogenation to produce fuels and value-added chemicals is a promising route to mitigate the energy crisis and global environmental issues caused by the excessive consumption of fossil fuels.[1–9] This newly developed technique can effectively broaden the utilization of the solar spectrum, especially low-energy infrared light that is often wasted in photochemical catalysis.[10–12] Moreover, compared with thermocatalytic processes, photo-excited energetic hot electrons or charge carriers can trigger the chemical reactions of adsorbed reactants under milder reaction conditions.[13–16] Generally, an ideal photothermal catalyst needs to satisfy the following criteria: good sunlight harvesting ability over the entire solar spectrum, high intrinsic catalytic activity, and ideal thermal management to prevent heat dissipation.[17] Despite substantial progress in the development of photothermal catalytic materials, most catalysts fail to meet all of the above requirements at the same time. There is still an urgent need to create more efficient catalytic systems.

Supported metal catalysts are widely used in photothermal CO_2 catalysis.[18,19] Structural engineering of metals and supports provides an effective way to optimise photothermal catalytic properties.[20,21] For example, classical nanoarray-structured materials have been widely used as a typical kind of substrate in photothermal catalysis due to their unique anti-reflective effects.[22] Furthermore, combined with the surface plasmon resonance (SPR) effect of loaded metal nanoparticles, nanoarray-based catalysts often exhibit excellent light-absorption ability.[23] Initially, Ozin and his co-workers reported a Ru/SiNW photothermal catalyst that uses black silicon nanowire arrays as supports to enhance light absorbance.[24] Recently, our group has developed a catalyst with plasmonic superstructure nanoarrays that can maximize the utilization of the entire sunlight spectrum.[25] However, poor dispersity of active metal nanoparticles in these catalysts contributed to poor intrinsic reactivity. Typically, the metals of array-based catalysts are loaded by magnetron sputtering.[26,27] Although tuning the sputtering deposition conditions can reduce the particle size, the straight up-and-down structure of nanowire and nanorod arrays will inevitably cause a wider distribution of metal particles. Agglomeration and overgrowth of metal nanoparticles can be found at the top of array structures, and these phenomena will also result in poor dispersity and low atomic utilization of decorated metals.[27,28] In addition, nanoarray structures and metal nanoparticles absorb light and act as active sites while the substrate beneath the arrays is almost useless for light absorption and catalysis but accelerates heat dissipation and weakens the catalytic performance. Therefore, it is still a big challenge to optimize nanoarray-based photothermal catalysts and obtain superior photothermal catalytic

[a]*Institute of Functional Nano & Soft Materials (FUNSOM), Soochow University, Suzhou, 215123 Jiangsu, PR China. E-mail: lehe@suda.edu.cn, crli@suda.edu.cn*
[b]*Jiangsu Key Laboratory of Advanced Negative Carbon Technologies, Soochow University, Suzhou, 215123 Jiangsu, PR China*
[c]*School of Optoelectronic Science and Engineering, Key Laboratory of Advanced Optical Manufacturing Technologies of Jiangsu Province, Key Laboratory of Modern Optical Technologies of Education Ministry of China, Soochow University, Suzhou, 215123, PR China. E-mail: zhangbingchang@suda.edu.cn*
† Electronic supplementary information (ESI) available. See DOI: https://doi.org/10.1039/d2nr02680e

This journal is © The Royal Society of Chemistry 2022

Published on 19 July 2022. Downloaded on 5/31/2024 7:48:38 PM.

performance with enhanced dispersion of active sites and good light-to-heat conversion properties.

Herein, we report the use of silicon nanocone arrays (SiNCs) as supports to increase the dispersity of Co nanoparticles. A thinning strategy to further improve light-to-heat conversion was also studied. Due to the combination of good light absorption, high metal dispersity, and low heat dissipation, the photothermal CO_2 conversion rate of the optimized catalyst (120 μm-SiNCs@Co) reached as high as 1780 mmol g_{Co}^{-1} h^{-1}. Our research reveals the importance of optimizing the dispersion of metal nanoparticles *via* structural engineering and improving the photothermal conversion of the system *via* heat management to maximize the photothermal catalytic performance.

Experimental

Chemicals

Hydrogen peroxide (H_2O_2, 30%) and silver nitrate ($AgNO_3$, 99.8%) were purchased from Shanghai Lingfeng Chemical Reagent Co., Ltd. Hydrofluoric acid (HF, 40 wt%) was obtained from Sinopharm Chemical Reagent Co., Ltd. All samples were prepared from p-type, double-sided polished (100) silicon wafers of different thicknesses with a resistivity of 1–10 Ω cm purchased from Zhejiang Lijing Co., Ltd. All chemicals were used as received without any further purification. Deionized water with a resistivity of 18.2 MΩ cm was used in all the experiments.

Synthesis of SiNCs and silicon nanowire arrays (SiNWs)

SiNCs and SiNWs were obtained through an all-wet metal-assisted chemical etching (MACE) method. Generally, the (100)-oriented p-type silicon wafers of different thicknesses were cut into 2 × 2 cm^2 squares and then ultrasonically cleaned in acetone, ethanol, and deionized water. Subsequently, the wafers were immediately placed into a silver deposition solution consisting of 4.8 M HF and 0.02 M $AgNO_3$, and sedimented for 120 s for SiNCs and 20 s for SiNWs. After the silicon wafers were coated with an even layer of Ag nanoparticles, they were then immediately placed into an etching solution containing 4.8 M HF and 0.4 M H_2O_2 for 15 min at room temperature. When the etching process was completed, the silicon wafers were washed repeatedly with deionized water. To thoroughly remove Ag nanoparticles, the wafers were immersed in concentrated nitric acid for 15 min and then rinsed with water and dried under N_2 flow.

Synthesis of SiNCs@Co and SiNWs@Co

Co was sputtered onto the above-obtained 4 cm^2 square SiNCs and SiNWs. The deposition was carried out in a custom-built sputtering system (Kurt J. Lesker Co.) *via* radio frequency (RF) magnetron sputtering using a 99.95% pure Co sputtering target purchased from Zhongnuo Advanced Material Co., Beijing China. The base pressure of the sputtering chamber was pumped down to 2 × 10^{-5} Torr before argon was introduced into the chamber at a flow rate of 10 sccm. The forward power was 100 W and the substrate to target distance was 17.5 cm. The sputtering amount was controlled by sputtering time.

Characterization

All the scanning electron microscopy (SEM) images were obtained using a Zeiss G500 instrument (from Carl Zeiss, Germany). All the transmission electron microscopy (TEM) images were obtained using a TECNAI G2 TEM operated at 200 kV. The data of diffuse reflectance spectra (DRS) were collected using a Lambda 950 ultraviolet–vis–near infrared (UV–vis–NIR) spectrometer from PerkinElmer with the spectrum ranging from 250 to 2500 nm. The loading amount of cobalt element on SiNCs and SiNWs was measured using an inductively coupled plasma source mass spectrometer (ICP-MS, Aurora M90, Jenoptik).

Photocatalytic testing

The gas-phase photothermal CO_2 reduction rate was measured in a transparent glass batch reactor with an annular sealed glass cover. After vacuum pumping the reaction system, a mixture of CO_2 and H_2 (1 : 1) was introduced into the reactor to reach 1 bar, and the reaction was monitored using an MIK-P300 pressure transducer. The photothermal CO_2 conversion was driven by a 300 W Xe arc lamp with 4 cm^2 samples located in the centre of the reactor. The power intensity of light was measured using a Spectra-Physics power meter to be 2.5 W cm^{-2} (≈25 suns) without any filters. The contents of product gases (CO and CH_4) in the reaction system were measured by gas chromatography (GC7900, Techcomp) with a flame ionization detector (FID) connected to a catalytic converter. The reaction time was set to be 20 min. Surface temperatures of different samples under light irradiation were measured using a digital thermocouple, which was placed on the surface of catalysts, and recorded online.

Results and discussion

Minimizing the excessive deposition of metal particles at the top of nanoarray structures could be useful in optimizing metal dispersity. Intuitively, nanocones are a good choice due to the reduced cross-sectional area at the top and fully exposed sides during the sputtering process. Experimentally, we first prepared SiNCs through a modified MACE method.[29] After precisely controlling the metal Ag deposition, a reasonable etching time of 15 min was chosen for the formation of SiNCs. Due to the unequal reaction rate between the cathode reaction and the anode reaction in the formed microscopic galvanic cells of Ag and Si, an additional Ag etching process occurs in which the size of Ag particles gradually decreased as shown in Fig. 1a, leading to the successful formation of SiNCs. The SEM images of the as-prepared Si nanocone array viewed from different directions are shown in Fig. 1b and c. The silicon nanocones were distributed all over the Si substrate surface

Published on 19 July 2022. Downloaded on 5/31/2024 7:48:38 PM.

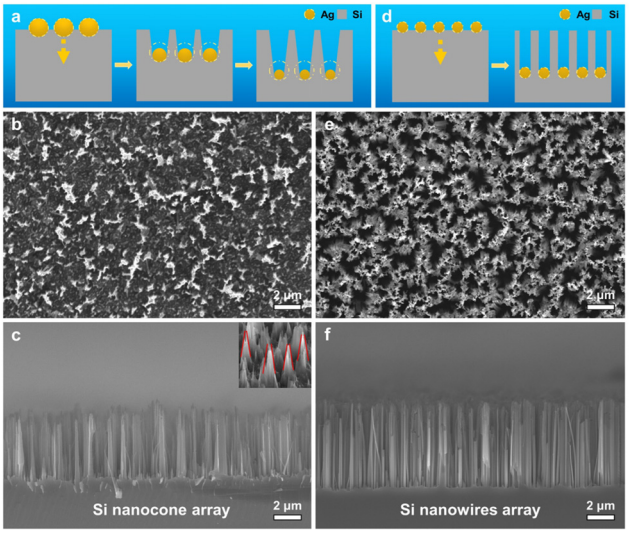

Fig. 1 (a) Schematic illustration of the formation process of SiNCs. (b) Top-view and (c) cross-sectional-view SEM images of SiNCs. The inset shows the localized 45° oblique-view SEM image of SiNCs. (d) Schematic illustration of the formation process of SiNWs. (e and f) SEM images of SiNWs viewed from different directions.

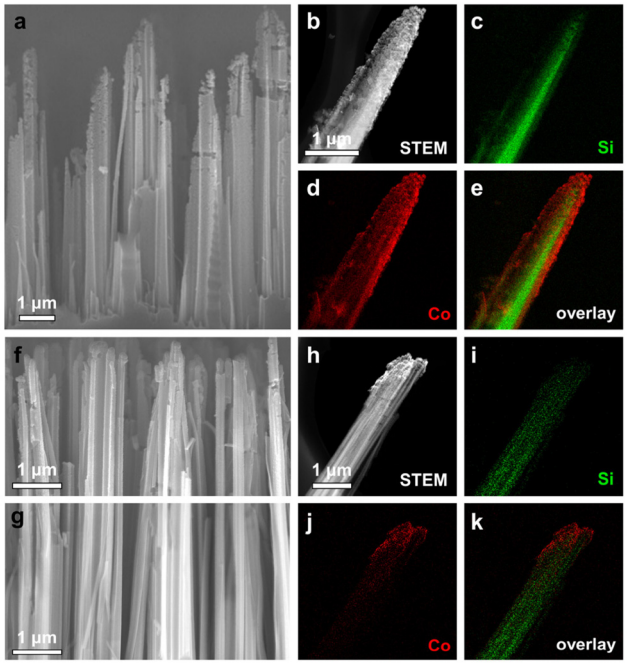

Fig. 2 (a) Cross-sectional-view SEM image of SiNCs@Co-1. (b) Scanning transmission electron microscopy (STEM) and (c–e) elemental mapping images of SiNCs@Co-1. SEM images of the (f) top and (g) bottom regions of SiNWs@Co-1. (h) STEM and (i–k) elemental mapping images of SiNWs@Co-1.

and are relatively uniform in length (4.7 ± 0.2 μm, Fig. S1†). The enlarged SEM image from a 45° oblique view in the inset of Fig. 1c indicates that the morphology of the obtained nanocones features tips on each head. For comparison, we prepared SiNWs *via* the typical MACE procedure in which Ag particles only act as a catalyst for silicon etching (Fig. 1d). Fig. 1e and f show SEM images featuring the top and cross-sectional views of SiNWs. It can be seen that the nanowires are more densely distributed on the silicon wafer than the nanocones (Fig. 1b and e). The front-row nanowires indicate that the average length of the nanowires was 5.8 ± 0.2 μm (Fig. S2†).

Cobalt was then loaded on the surface of both nanoarray structures by magnetron sputtering under vacuum. According to our previous research, the optimal sputtering time of 15 min was first employed.[23] The as-prepared composite catalysts are denoted as SiNCs@Co-1 and SiNWs@Co-1 (Fig. S3†). As shown in Fig. 2a, the entire surface of SiNCs@Co-1 became rough, confirming that the metal particles were successfully dispersed. TEM was used to further observe the Co nanoparticles. As we expected, 3.7 ± 0.9 nm particles were free from overgrowth and evenly distributed on the Si nanocones (Fig. S4†). In contrast, the top regions of SiNWs@Co-1 were clearly rougher than the bottom regions (Fig. 2f and g). Moreover, the energy dispersive X-ray (EDX) mapping results further confirm the successful preparation of SiNCs@Co-1 and SiNWs@Co-1 (Fig. 2b–e and h–k). Obviously, SiNCs can facilitate a better distribution of Co nanoparticles than SiNWs with Co tending to accumulate on the top region. Samples with different loading amounts were obtained by controlling the sputtering time. Two samples with longer sputtering time (25 min) were also prepared, denoted as SiNCs@Co-2 and SiNWs@Co-2 (Fig. S5 and S6†). The actual loading amounts of cobalt element were measured by ICP-MS with 0.16 mg for 15 min sputtering and 0.29 mg for 25 min sputtering. The above results clearly demonstrate the effectiveness of our structural-engineering strategy in improving the dispersity of metal particles.

Light harvesting ability is an important factor to evaluate the quality of a photothermal catalyst. Therefore, UV–vis–NIR DRS was used to assess the light absorption ability of the composite catalysts before carrying out catalytic tests. We first evaluated the light absorbance of nanoarray substrates. Although the length of SiNCs is shorter than that of SiNWs, the light absorption abilities of these two arrays are nearly the same and are much stronger than those of planar Si wafers in the 250–1100 nm wavelength region (Fig. S7†). After loading Co nanoparticles, the absorbance was greatly improved, especially in the NIR region (Fig. 3a). Overall, the composite catalysts exhibited strong light-absorption ability over the entire solar spectrum due to the combination of the light-trapping effect of the nanoarray structures and the SPR of Co nanoparticles. This means that the catalysts can achieve efficient utilization of the full solar spectrum, which will be beneficial for obtaining good photothermal catalytic performance.

Testing of photothermal catalytic CO_2 conversion was conducted at room temperature in a batch reactor with a gas mixture ($CO_2 : H_2$ = 0.5 bar : 0.5 bar). A 300 W Xe lamp was used to simulate the concentrated sunlight and the intensity of incident light was adjusted to 25 suns. In order to exclude any effects that the supports may have had, catalytic tests of SiNCs and SiNWs were first conducted. After reacting for

 This journal is © The Royal Society of Chemistry 2022

Published on 19 July 2022. Downloaded on 5/31/2024 7:48:38 PM.

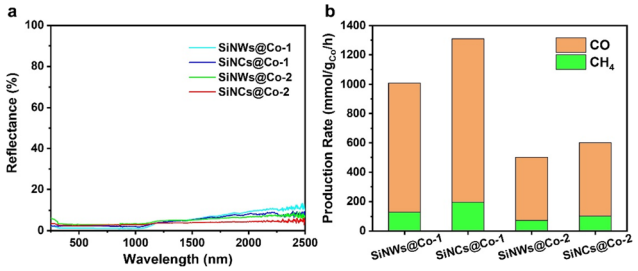

Fig. 3 (a) Diffuse reflectance spectra and (b) photothermal catalytic performances of SiNCs@Co-1, SiNWs@Co-1, SiNCs@Co-2 and SiNWs@Co-2.

20 min, no products were detected within the limits of the gas chromatography instrument, suggesting that the pure Si arrays are inert for CO_2 hydrogenation (Fig. S8†). Afterwards, we investigated the catalytic performance of the aforementioned composite catalysts. Before carrying out the catalytic tests, the chemical states of surface cobalt in SiNCs@Co were investigated by X-ray photoelectron spectroscopy (XPS). The Co $2p_{3/2}$ and $2p_{1/2}$ peaks are located at 778.3 and 793.8 eV, respectively, which can be assigned to metallic cobalt (Fig. S9†). Additional peaks located at higher binding energies (780.7 and 797.2 eV) for Co 2p are likely to be Co in CoO_x due to the inevitable exposure of the sample to air during the XPS test. Furthermore, a hydrogen temperature programmed reduction (H_2-TPR) experiment was performed. As shown in Fig. S10,† there are two peaks of 203 °C and 357 °C on the H_2-TPR curve, which can be assigned to the reduction of weakly bonded Co^{3+} species and CoO_x, respectively. As the samples for catalytic tests are freshly prepared and light irradiation under working conditions will also help in promoting the reduction of surface-oxidized Co, the working state of cobalt in SiNCs@Co is mainly Co^0. Since the contributors of catalytic activity are mainly Co nanoparticles, the CO_2 conversion rate (R_{CO_2}) was normalized by the mass of Co for better comparisons among the samples. SiNCs@Co-1 exhibited a R_{CO_2} of 1310 mmol g_{Co}^{-1} h^{-1}, which was about 300 mmol g_{Co}^{-1} h^{-1} higher than that of SiNWs@Co-1 under similar metal loading, light utilization, and surface temperature (Fig. 3 and Fig. S11†). The rate difference can be attributed to the intrinsic activity arising from the difference in metal dispersity. Notably, SiNCs@Co-2 and SiNWs@Co-2 with higher Co loading amounts showed better light absorption, but the dramatic decrease in activity further emphasizes the importance of metal dispersity.

The SEM images can be used to further evaluate the catalytic performance of the catalysts. Due to the straight up-and-down structure and the small intervals between the nanowires, the sputtered Co nanoparticles are mainly concentrated at the upper part of SiNWs (Fig. 2f and Fig. S3b†). Large particles accumulate mostly at the top of the structure while the rest of SiNWs look smooth, as if there was a complete absence of Co nanoparticles (Fig. 2g). In contrast, SiNCs can facilitate better distribution of Co nanoparticles over the entire structure and thus can expose more active sites due to the larger intervals between the nanocones (Fig. S3a†), resulting in a higher catalytic activity than SiNWs@Co with the same loading amount. Unfortunately, although the SiNC structure serves to improve the Co nanoparticle dispersion, the increase in the loading amount will still inevitably lead to agglomeration and overgrowth of Co nanoparticles both on SiNCs and SiNWs (Fig. S5 and S6†), lowering the atomic utilization and catalytic activity. Meanwhile, an increase in the loading amount also leads to a small decrease of CO selectivity which further indicates the overgrowth of Co nanoparticles. The results reveal that optimizing the dispersion of metal nanoparticles on the supports plays a crucial role in improving the photothermal catalytic activity.

It is clear that the SiNCs@Co-1 composite catalyst exhibits strong light absorption ability over the full solar spectrum and fairly strong catalytic activity. Our previous study has shown the importance of substrate effects on the activity of photothermal catalysts. The Si substrate in the composite catalyst system is a material with good thermal conductivity (149 W m^{-1} K^{-1}) but may be partially responsible for the heat loss.[30] On the basis of this, it is reasonable to thin the Si substrate (Fig. 4a), thus reducing this loss, improving light-to-heat conversion and further increasing the photothermal catalytic activity. Therefore, we chose SiNCs@Co-1, which exhibited the highest activity in all the above samples, replaced the SiNCs etched from 480 μm Si wafers with 210 μm and 120 μm ones, and then carried out photothermal catalytic tests under the same conditions (Fig. 4b–d). Considering that the change of substrate thickness may affect the light absorption of composite catalysts, DRS of the three catalysts was first performed. Fig. 4e shows the near-coincident curves of the three catalysts with different Si substrate thicknesses, indicating that the light absorption ability is mainly determined from the nanoarray structure and loading amount of metals. Meanwhile, the results of the catalytic tests show that a smaller thickness of the Si substrate will lead to a higher photothermal catalytic activity (Fig. 4f). Surprisingly, 120 μm-SiNCs@Co-1 exhibits the highest R_{CO_2} of 1780 mmol g_{Co}^{-1} h^{-1} among the reported Co-based photothermal catalysts (Table 1). Fig. 4g shows the surface temperature profiles of different catalysts under 25-sun irradiation. Likewise, it shows that a higher surface temperature of the composite catalyst can be obtained with a smaller thickness of the Si substrate. Moreover, a smaller thickness of the Si substrate will also lead to a slightly higher CO selectivity because the reverse water gas shift (RWGS: $CO_2 + H_2 \rightarrow CO + H_2O$) is a typical endothermic reaction and a higher temperature will facilitate the reaction. This indicates that the strategy of thinning the substrate can indeed reduce the heat loss and thus increase the photothermal catalytic activity, which is consistent with our hypothesis.

To further verify the thinning strategy, we also reduced the substrate thickness of SiNWs@Co-1 from 485 μm to 210 μm and 120 μm and then tested the light absorbance (Fig. S12†), photothermal catalytic activity (Fig. S13†) and surface temperature (Fig. S14†) of the catalysts. The results are consistent with the patterns exhibited by the catalysts with SiNCs of different substrate thicknesses as supports. Overall, the results empha-

Published on 19 July 2022. Downloaded on 5/31/2024 7:48:38 PM.

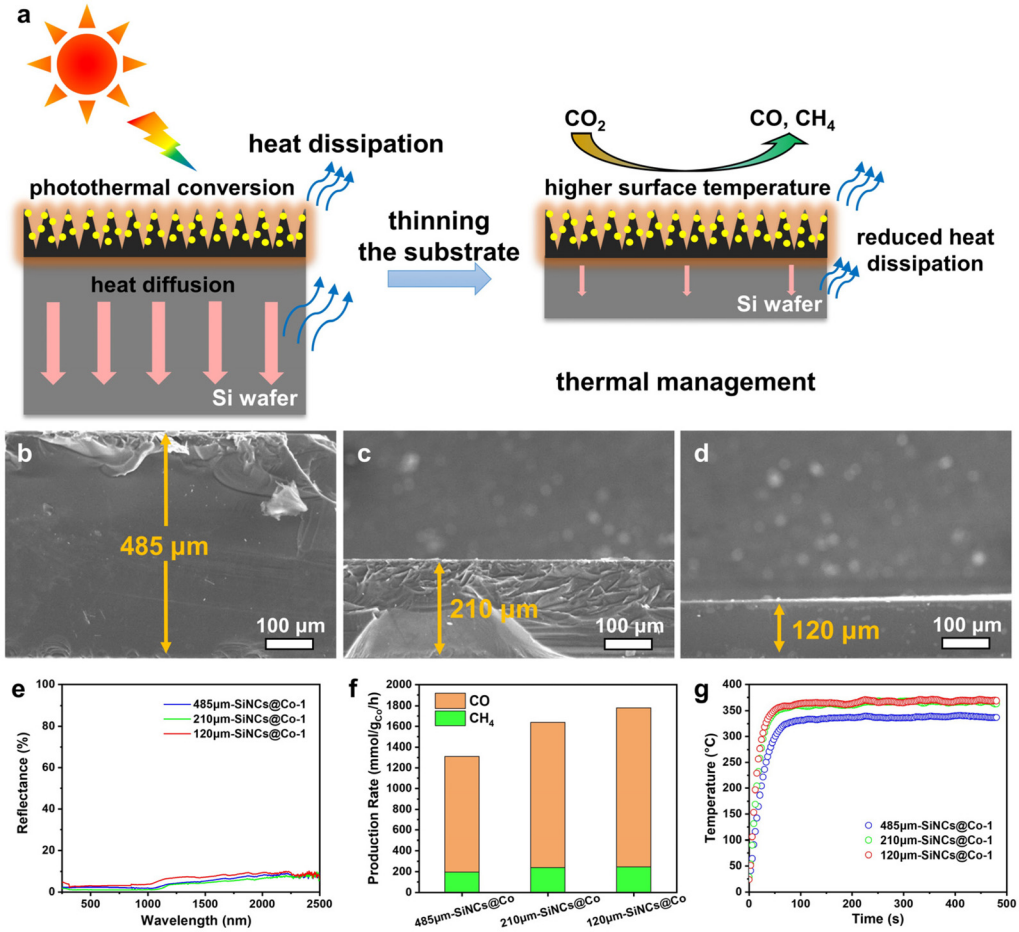

Fig. 4 (a) Schematic illustration of the thinning strategy for thermal management in photothermal catalysis. (b–d) SEM images of Si substrates with different thicknesses. (e) Diffuse reflectance spectra, (f) catalytic performances and (g) surface temperatures of nanocone array-based catalysts with different substrate thicknesses.

Table 1 Performance of various cobalt catalysts in photothermal CO_2 hydrogenation

Catalyst	Light source	$H_2 : CO_2$	R_{max} [mmol g_{Co}^{-1} h^{-1}]	Ref.
SNAs@Co	300 W Xe light (2.5 W cm^{-2})	1 : 1	433	23
Co–PS@SiO_2	300 W Xe light (2.0 W cm^{-2})	1 : 1	612.4	25
Co@dpAAO-400	300 W Xe light (2.5 W cm^{-2})	1 : 1	1666	27
Co@SiO_2-array	300 W Xe light (2.4 W cm^{-2})	1 : 1	407.3	28
Co/Al_2O_3	300 W Xe light	4 : 1	900	31
Co@CoN&C-1	300 W Xe light	1 : 1	144.9	32
Co–SiO_2	300 W Xe light (2.7 W cm^{-2})	1 : 1	1522	33
120 μm-SiNCs@Co	300 W Xe light (2.5 W cm^{-2})	1 : 1	1780	This work

size the importance of thermal management in reducing heat dissipation and improving both photothermal conversion and catalytic activity in photothermal catalysis.

Conclusions

In summary, we have developed a low-cost and efficient nanoarray-based photothermal catalyst with improved metal particle dispersion and heat management using a thinned nanocone array as the substrate. As this helped in boosting the photothermal catalytic performance of Co-based catalysts, this indicates that silicon nanocones can be promising supports for photothermal catalysis. Atomic layer deposition (ALD) might be used in future research to achieve more precise structural engineering and thus obtain both higher catalytic activity and better control over selectivity. It is also important to note that a silica coating strategy can be integrated into this system against sintering under working conditions (Fig. S15†) to improve the activity and durability of the catalysts under more

 This journal is © The Royal Society of Chemistry 2022

intense light.[34,35] This work reveals the importance of optimizing the dispersion of active sites *via* structural engineering and improving the photothermal conversion of the system *via* thermal management for enhanced photothermal catalytic performance. The general strategy can be extended to other nanoarray catalysts, laying a foundation for efficient photothermal catalytic CO_2 reduction.

Conflicts of interest

There are no conflicts to declare.

Acknowledgements

This work was financially supported by the National Natural Science Foundation of China (51920105005, 52172221, 21902113, and 51821002), the Natural Science Foundation of Jiangsu Province (BK20200101), the National Key R&D Program of China (2021YFF0502000), the National Postdoctoral Program for Innovative Talents (BX20220222), the China Postdoctoral Science Foundation (2021M702388), the Jiangsu Key Laboratory for Carbon-Based Functional Materials and Devices (ZZ2103), Suzhou Key Laboratory of Functional Nano & Soft Materials, Collaborative Innovation Center of Suzhou Nano Science & Technology, the 111 Project, Joint International Research Laboratory of Carbon-Based Functional Materials and Devices.

Published on 19 July 2022. Downloaded on 5/31/2024 7:48:38 PM.

References

1 M. Cai, Z. Wu, Z. Li, L. Wang, W. Sun, A. A. Tountas, C. Li, S. Wang, K. Feng, A.-B. Xu, S. Tang, A. Tavasoli, M. Peng, W. Liu, A. S. Helmy, L. He, G. A. Ozin and X. Zhang, *Nat. Energy*, 2021, **6**, 807–814.
2 Y. Chen, Y. Zhang, G. Fan, L. Song, G. Jia, H. Huang, S. Ouyang, J. Ye, Z. Li and Z. Zou, *Joule*, 2021, **5**, 3235–3251.
3 Y. Yao, L. Wang, X. Zhu, W. Tu, Y. Zhou, R. Liu, J. Sun, B. Tao, C. Wang, X. Yu, L. Gao, Y. Cao, B. Wang, Z. Li, W. Yao, Y. Xiong, M. Yang, W. Wang and Z. Zou, *Joule*, 2022, **6**(5), 1008–1014.
4 D. Mateo, J. L. Cerrillo, S. Durini and J. Gascon, *Chem. Soc. Rev.*, 2021, **50**, 2173–2210.
5 T. Kong, Y. Jiang and Y. Xiong, *Chem. Soc. Rev.*, 2020, **49**, 6579–6591.
6 E. C. Ra, K. Y. Kim, E. H. Kim, H. Lee, K. An and J. S. Lee, *ACS Catal.*, 2020, **10**, 11318–11345.
7 K. Feng, J. Tian, M. Guo, Y. Wang, S. Wang, Z. Wu, J. Zhang, L. He and B. Yan, *Appl. Catal., B*, 2021, **292**, 120191.
8 L. Wang, M. Ghoussoub, H. Wang, Y. Shao, W. Sun, A. A. Tountas, T. E. Wood, H. Li, J. Y. Y. Loh, Y. Dong, M. Xia, Y. Li, S. Wang, J. Jia, C. Qiu, C. Qian, N. P. Kherani, L. He, X. Zhang and G. A. Ozin, *Joule*, 2018, **2**, 1369–1381.
9 Y. Zhao, W. Gao, S. Li, G. R. Williams, A. H. Mahadi and D. Ma, *Joule*, 2019, **3**, 920–937.
10 M. Ghoussoub, M. Xia, P. N. Duchesne, D. Segal and G. Ozin, *Energy Environ. Sci.*, 2019, **12**, 1122–1142.
11 N. Kong, B. Han, Z. Li, Y. Fang, K. Feng, Z. Wu, S. Wang, A.-B. Xu, Y. Yu, C. Li, Z. Lin and L. He, *ACS Appl. Nano Mater.*, 2020, **3**, 3028–3033.
12 Z. Wu, C. Li, Z. Li, K. Feng, M. Cai, D. Zhang, S. Wang, M. Chu, C. Zhang, J. Shen, Z. Huang, Y. Xiao, G. A. Ozin, X. Zhang and L. He, *ACS Nano*, 2021, **15**, 5696–5705.
13 X. Wang, F. Wang, Y. Sang and H. Liu, *Adv. Energy Mater.*, 2017, **7**, 1700473.
14 L. Zhou, J. M. P. Martirez, J. Finzel, C. Zhang, D. F. Swearer, S. Tian, H. Robatjazi, M. Lou, L. Dong, L. Henderson, P. Christopher, E. A. Carter, P. Nordlander and N. J. Halas, *Nat. Energy*, 2020, **5**, 61–70.
15 Y. Tong, L. Song, S. Ning, S. Ouyang and J. Ye, *Appl. Catal., B*, 2021, **298**, 120551.
16 R. Kamarudheen, G. W. Castellanos, L. P. J. Kamp, H. J. H. Clercx and A. Baldi, *ACS Nano*, 2018, **12**, 8447–8455.
17 C. Song, Z. Wang, Z. Yin, D. Xiao and D. Ma, *Chem. Catal.*, 2021, **2**, 52–83.
18 G. Chen, R. Gao, Y. Zhao, Z. Li, G. I. N. Waterhouse, R. Shi, J. Zhao, M. Zhang, L. Shang, G. Sheng, X. Zhang, X. Wen, L. Z. Wu, C. H. Tung and T. Zhang, *Adv. Mater.*, 2018, **30**, 1704663.
19 Z. Li, X. Zhang, J. Liu, R. Shi, G. I. N. Waterhouse, X. D. Wen and T. Zhang, *Adv. Mater.*, 2021, **33**, 2103248.
20 T. Shao, X. Wang, H. Dong, S. Liu, D. Duan, Y. Li, P. Song, H. Jiang, Z. Hou, C. Gao and Y. Xiong, *Adv. Mater.*, 2022, **34**, 2202367.
21 F. Zhang, Y.-H. Li, M.-Y. Qi, Y. M. A. Yamada, M. Anpo, Z.-R. Tang and Y.-J. Xu, *Chem. Catal.*, 2021, **1**, 272–297.
22 L. B. Hoch, P. G. O'Brien, A. Jelle, A. Sandhel, D. D. Perovic, C. A. Mims and G. A. Ozin, *ACS Nano*, 2016, **10**, 9017–9025.
23 D. Zhang, K. Lv, C. Li, Y. Fang, S. Wang, Z. Chen, Z. Wu, W. Guan, D. Lou, W. Sun, D. Yang, L. He and X. Zhang, *Sol. RRL*, 2020, **4**, 2000387.
24 P. G. O'Brien, A. Sandhel, T. E. Wood, A. A. Jelle, L. B. Hoch, D. D. Perovic, C. A. Mims and G. A. Ozin, *Adv. Sci.*, 2014, **1**, 1400001.
25 K. Feng, S. Wang, D. Zhang, L. Wang, Y. Yu, K. Feng, Z. Li, Z. Zhu, C. Li, M. Cai, Z. Wu, N. Kong, B. Yan, J. Zhong, X. Zhang, G. A. Ozin and L. He, *Adv. Mater.*, 2020, **32**, 2000014.
26 P. G. O'Brien, K. K. Ghuman, A. A. Jelle, A. Sandhel, T. E. Wood, J. Y. Y. Loh, J. Jia, D. Perovic, C. V. Singh, N. P. Kherani, C. A. Mims and G. A. Ozin, *Energy Environ. Sci.*, 2018, **11**, 3443–3451.
27 D. Lou, A. B. Xu, Y. Fang, M. Cai, K. Lv, D. Zhang, X. Wang, Y. Huang, C. Li and L. He, *ChemNanoMat*, 2021, **7**, 1008–1012.
28 Y. Fang, K. Lv, Z. Li, N. Kong, S. Wang, A. B. Xu, Z. Wu, F. Jiang, C. Li, G. A. Ozin and L. He, *Adv. Sci.*, 2020, **7**, 2000310.
29 C. Bian, B. Zhang, Z. Zhang, H. Chen, D. Zhang, S. Wang, J. Ye, L. He, J. Jie and X. Zhang, *ACS Omega*, 2022, **7**, 2234–2243.

30 M. Cai, C. Li and L. He, *Rare Met.*, 2020, **39**, 881–886.
31 X. Meng, T. Wang, L. Liu, S. Ouyang, P. Li, H. Hu, T. Kako, H. Iwai, A. Tanaka and J. Ye, *Angew. Chem., Int. Ed.*, 2014, **53**, 11478–11482.
32 S. Ning, H. Xu, Y. Qi, L. Song, Q. Zhang, S. Ouyang and J. Ye, *ACS Catal.*, 2020, **10**, 4726–4736.
33 X. Wang, Z. Zhu, Z. Wu, C. Zhang, Z. Chen, M. Xiao, C. Li and L. He, *J. Inorg. Mater.*, 2022, **37**, 22–28.
34 D. Lou, Z. Zhu, Y.-F. Xu, C. Li, K. Feng, D. Zhang, K. Lv, Z. Wu, C. Zhang, G. A. Ozin, L. He and X. Zhang, *Sci. China Mater.*, 2021, **64**, 2212–2220.
35 Z. Zhu, K. Feng, C. Li, R. Tang, M. Xiao, R. Song, D. Yang, B. Yan and L. He, *Adv. Mater.*, 2022, **34**, 2108727.

Published on 19 July 2022. Downloaded on 5/31/2024 7:48:38 PM.

This journal is © The Royal Society of Chemistry 2022